Identification of Lone-Pair Surface States on Indium Oxide

Daniel W. Davies,[†] Aron Walsh,[‡] James J. Mudd,[§,∥] Chris F. McConville,[§,⊥] Anna Regoutz,*,[‡] J. Matthias Kahk,[‡] David J. Payne,[‡] Vin R. Dhanak,[#] David Hesp,[#] Katariina Pussi,[∇] Tien-Lin Lee,[∥] Russell G. Egdell,[○] and Kelvin H. L. Zhang*,[◆]

[†]Department of Chemistry, University of Bath, Bath BA2 7AY, United Kingdom

[‡]Department of Materials, Imperial College London, Exhibition Road, London SW7 2AZ, United Kingdom

[§]Department of Physics, University of Warwick, Coventry CV4 7AL, United Kingdom

[∥]Diamond Light Source Ltd., Didcot, Oxfordshire OX11 ODE, United Kingdom

[⊥]School of Science, RMIT University, Melbourne, Victoria 3001, Australia

[#]Department of Physics, University of Liverpool, Liverpool L69 3BX, United Kingdom

[∇]LUT School of Engineering Science, Lappeenranta University of Technology, P.O. Box 20, FIN-53851 Lappeenranta, Finland

[○]Department of Chemistry, Inorganic Chemistry Laboratory, University of Oxford, South Parks Road, Oxford OX1 3QR, United Kingdom

[◆]State Key Laboratory of Physical Chemistry of Solid Surfaces, College of Chemistry and Chemical Engineering, Xiamen University, Xiamen 361005, People's Republic of China

S *Supporting Information*

ABSTRACT: Indium oxide is widely used as a transparent electrode in optoelectronic devices and as a photocatalyst with activity for reduction of CO_2. However, very little is known about the structural and electronic properties of its surfaces, particularly those prepared under reducing conditions. In this report, directional "lone-pair" surface states associated with filled $5s^2$ orbitals have been identified on vacuum-annealed $In_2O_3(111)$ through a combination of hard and soft X-ray photoemission spectroscopy and density functional theory calculations. The lone pairs reside on indium ad-atoms in a formal +1 oxidation state, each of which traps two electrons into a localized hybrid orbital protruding away from the surface and lying just above the valence band maximum in photoemission spectra. The third electron associated with the ad-atoms is delocalized into the conduction band, thus producing the surface electron accumulation layer identified previously on vacuum-annealed $In_2O_3(111)$ (1×1) surfaces. The surface structure is further supported by low-energy electron diffraction, but there is no chemical shift in indium core level X-ray photoelectron spectra between surface In(I) ad-atoms and bulk In(III). The $5s^2$ lone pairs confer Lewis basicity on the surface In sites and may have a pronounced impact on the catalytic or photocatalytic activity of reduced In_2O_3.
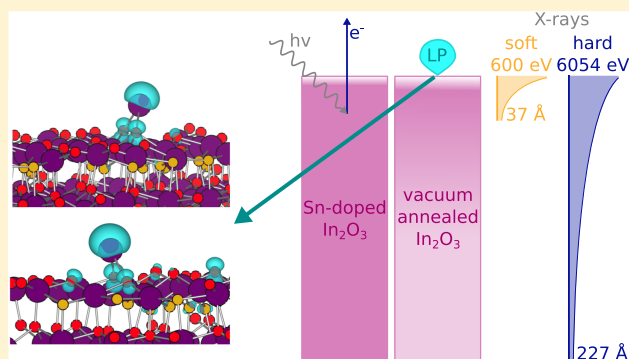
1. INTRODUCTION

Metallic elements occupying positions beyond the end of the transition series in the periodic table display two main oxidation states: the group oxidation state N and the N-2 state.[1,2] Lower valent N-2 compounds frequently adopt structures in the solid state where the N-2 cations occupy sites with coordination geometries lacking inversion symmetry: Sn(II)O,[3] Sn(II)S,[4] Pb(II)O,[5] and Bi(III)$_2$O$_3$[6] are just some typical examples. Free ions in the N-2 state such as Sn^{2+} have an ns^2 electron configuration, with empty np levels. The conventional explanation of the propensity for asymmetric cation sites involves the idea of directional electron "lone pairs" formed by on-site hybridization between occupied metal ns states and one of the empty np states, thus lowering the

internal electronic energy of the cation through the second-order Jahn−Teller effect.[1,2] This mixing is not possible at sites with inversion symmetry because s and p states are of opposite parity. However, the metal ns states are generally much too low in energy to allow direct interaction with metal np states.[7,8] Through a combination of first-principles calculations and X-ray spectroscopy techniques, it has been shown recently that the ns−np interaction must instead be mediated by anion states, whose energy lies between that of the ns and np

states.[9,10] Nonetheless, the idea of directional lone-pair hybrid states as the drivers of the structural distortions remains valid.

Cations occupying sites at a surface cannot experience full inversion symmetry. Moreover, oxides such as $Sn(IV)O_2$ and $In(III)_2O_3$ have a propensity toward electron-rich n-type behavior, with the facile formation of oxygen vacancies. Bulk oxygen vacancies are two electron donors, although whether this donor is deep or shallow is a matter of ongoing debate.[11,12] At a surface, it may be envisaged that the electrons could be trapped in a directional lone-pair state protruding out into the vacuum from a surface cation adjacent to an oxygen vacancy.[13] Lone-pair surface states of this sort were first invoked to account for structure in the bandgap of photoemission spectra of $Sn(IV)O_2$.[14−18] More recently, Ga(I) lone pairs have been used to rationalize structure in photoemission spectra of ion-bombarded $Ga(III)_2O_3$.[19] Lone-pair surface states have also been invoked to account for the photocatalytic reduction of CO on In_2O_3 powders.[13] Nonetheless, unambiguous identification of a lone-pair state on a structurally well-defined oxide surface through a combination of theory and experiment has remained elusive.

Here, an electronic state in the bulk bandgap of vacuum-annealed $In_2O_3(111)$ (1×1) is characterized by combined soft and hard X-ray photoemission measurements.[20] Indium oxide adopts the bixbyite structure, based on a $2 \times 2 \times 2$ supercell of the fluorite (CaF_2) structure with an ordered arrangement of 25% of the anion sites, which are empty. As with fluorite, the (111) surface is the most stable amongst the low index terminations and is based on repeating quadrupolar units with stoichiometry $\{O_{12}In_{16}O_{12}\}$ and a single dangling bond for each atom at the surface. Previous analysis of intensity−voltage (I/V) curves in low-energy electron diffraction (LEED) for $In_2O_3(111)$ (1×1) assumed an essentially bulk-truncated structure with minor relaxations.[21] However, more recent work using scanning tunneling microscopy (STM) has shown that there are in fact two distinct (1×1) structures: the bulk-truncated structure assumed in the previous LEED I/V study and a new structure containing a single indium ad-atom within each surface unit cell. The latter is formed by annealing under ultrahigh vacuum (UHV)[22] or by deposition of Fe.[23] The signature of the ad-atom reconstruction, a hexagonal array of bright spots in STM, was found in our own work using surface preparation procedures similar to those in the LEED experiments.[24] This has prompted reanalysis of our previously published LEED data. Addition of an ordered array of indium ad-atoms to the bulk−cut structure leads to a small but significant improvement in the Pendry R-factor. Density functional theory (DFT) calculations confirm that the occupation of 3-fold hollow sites by the ad-atoms used in the LEED analysis is energetically favored. As a result, simple electron counting dictates that each additional In atom (whose electron configuration is $5s^2 5p^1$) must contribute three electrons to the slab. It emerges that two of these electrons are trapped on the In ad-atoms in a directional In(I) lone-pair surface state, whereas the third electron gives rise to an electron accumulation layer that has been characterized previously by both angle-integrated[25,26] and angle-resolved photoemission spectroscopy (ARPES) measurements.[27] Thus, both the states in the bulk bandgap and the electrons in the accumulation layer are associated with indium(I) ad-atoms. This conclusion differs from the previous interpretation of ARPES data based on the theoretical results of Lany et al.,[11] where it was argued that the accumulation

layer arose from shallow surface oxygen vacancy donors, and the gap feature was assigned to deeper lying bulk oxygen vacancy states.[27] Note that since O-vacancies are two electron donors, the same vacancy cannot be responsible for both two-electron lone-pair states in the bandgap and electrons in the accumulation layer.

2. EXPERIMENTAL AND COMPUTATIONAL METHODS

Undoped In_2O_3 and 3% Sn-doped In_2O_3 (ITO) single-crystal thin films with atomically flat surfaces were grown on Y-$ZrO_2(111)$ substrates in an oxide molecular beam epitaxy (MBE) system at a substrate temperature of 700 °C with an oxygen plasma pressure of 3×10^{-5} mbar to a thickness of 210 nm.[28] The initial carrier concentrations for the as-grown In_2O_3 and ITO films were 2×10^{18} and 4×10^{20} cm^{-3}, respectively, as determined by Hall measurements and further confirmed by infrared reflectivity. The carrier density increased to a higher value of around 1.5×10^{19} cm^{-3} for the undoped sample after the experimental measurements in UHV, a value above the limit for the onset of degeneracy. For the Sn-doped sample, it was possible to estimate an in situ carrier density of around 4.5×10^{20} cm^{-3} from measurement of a plasmon satellite on the In 3d core line at 0.6 eV (see below).[29]

Valence and core-level photoemission spectra were obtained at the I09 beamline of the Diamond Light Source, U.K. This beamline delivers photons with energies ranging from 100 to 18 000 eV using two canted undulators, providing both soft and hard X-rays focused to the same point on the sample. Hard X-rays ($h\nu$ = 6054 eV) were selected using a cooled Si(111) double-crystal monochromator coupled with an additional channel-cut Si(004) high-resolution monochromator. Soft X-rays ($h\nu$ = 600 eV) were obtained using a plane grating monochromator (300 lines/mm). The end station is equipped with a VG Scienta EW4000 electron analyzer with ±30° angular acceptance. The photon beam is perpendicular to the electron emission direction. The photon beam is polarized in the plane of the orbit (horizontally) resulting in the electric vector being aligned with the electron emission direction. The sample was placed in a grazing incidence geometry (∼10°), with the surface normal in the plane defined by the photon beam and electron emission direction (p-polarized), thereby significantly enhancing the count rate. The experiments were performed at room temperature. The total experimental energy resolution was better than 0.6 eV for all photon energies. Experiments were conducted on an undoped sample, which had been previously annealed in oxygen,[27] and on the same sample after gentle Ar ion bombardment (6 mA, 500 eV for 5 min) followed by annealing at 500 °C for 30 min in UHV. An as-presented Sn-doped sample was studied for comparison. The UHV-annealed In_2O_3 sample gave a well-defined (1×1) LEED pattern, as discussed in Section 3.3. The endstation of the I09 beamline does not include facilities for STM or for measurement of LEED I/V curves. However, our previous measurements on an MBE-grown In_2O_3 thin film in different UHV chambers connected directly with STM showed the appearance of the ordered bright dots (as shown in Figure S1 in Supporting Information),[24] characteristic of the In ad-atoms reported by Wagner et al.[22] This earlier work involved in situ ion bombardment and annealing cycles similar to those of the current experiments. Also, the current experiments may be linked to the LEED I/V data set reported previously,[21] where measurements were performed on a sample grown in an
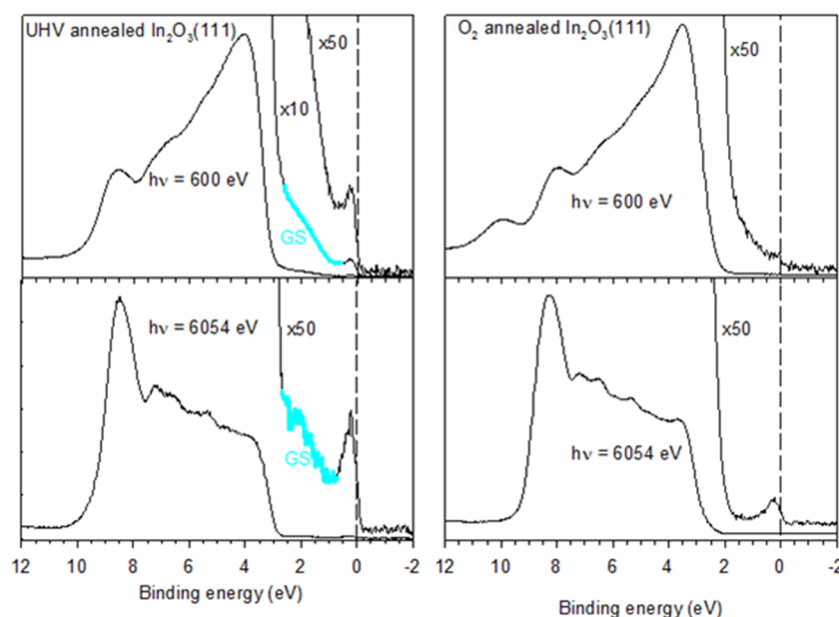
Figure 1. Hard and soft X-ray photoemission spectra of In_2O_3(111) after annealing in UHV (left panels) and after annealing in oxygen (right panels). The gap state (GS) that is the main focus of this paper is highlighted in cyan in the left hand panels. Note the factor of 5 difference in the expansions of the highlighted region for the data taken at the two different photon energies ($\times10$ at 600 eV and $\times50$ at 6054 eV).

identical fashion to that used in the current work and subject to the same in situ surface preparation procedures.

First-principles calculations were performed on the pristine (111) surface of In_2O_3, which is the lowest energy termination of the crystal, and contains planes of charge neutral $\{O_{12}In_{16}O_{12}\}$ trilayers. A slab model of 4 quadrupolar trilayers (160 atoms) was used, as previously reported.[30] The total energy and electronic structure were calculated within DFT as implemented in the Vienna ab initio simulation package (VASP) code, allowing for both lateral and vertical relaxations of all atoms in the slab. The total energy and electronic structure were calculated within DFT, as implemented in the VASP code. The electronic wavefunctions were represented using plane waves with a kinetic energy cutoff of 500 eV, and the Brillouin zone was sampled using a k-point grid of $2 \times 2 \times 1$ ($4 \times 4 \times 1$ for the density of states). Calculations were performed using the PBEsol exchange−correlation functional, allowing for both lateral and vertical relaxations of all atoms in the slab. The potential energy surface for indium ad-atom adsorption was assessed by introducing a 10×10 grid onto the (111) surface and calculating the total energy for a locally relaxed structure at each grid point.

The dynamical LEED calculations were performed using the Tensor-LEED program.[31] The relativistic phase shifts were calculated using the phase shift program that is packaged with Tensor-LEED.[32] The agreement between the theory and the experiment was tested using the Pendry R-factor, and the error bars quoted are calculated using the Pendry RR-function.[33] Four different sets of phase shifts were used: two for oxygen and two for indium. At the beginning of the analysis, the Debye temperatures were set to 108 K for In and 500 K for O. The l_{max} value was set to 8, and the imaginary part of inner potential was set to −5.0 eV. These values were optimized in the final stages of the analysis to 200 and 350 K for the surface (i.e., ad-atom) and bulk In, respectively; to 1000 and 2500 K for the surface and bulk O; to 8 for l_{max} and to −5.5 eV for imaginary part of inner potential. The real part of the inner

potential is independent of energy and was allowed to relax as is normal in LEED analysis.

3. RESULTS AND DISCUSSION

3.1. Valence Region Photoemission Spectra. Valence band photoemission spectra of vacuum-annealed In_2O_3(111) (1×1) excited at 600 and 6054 eV photon energy are shown in the left panels of Figure 1. The most obvious change in the spectra with increasing photon energy is pronounced enhancement in the relative intensity of the peak at the bottom of the valence band compared to other features in the spectra.

At the same time, a weak peak near the Fermi level shows more muted intensity enhancement relative to the top of the valence band. Finally, a broad shoulder toward the bottom of the bulk bandgap (identified as a gap state and marked as GS) in the figure decreases in intensity relative to both the Fermi level peak and the valence band maximum. Both the gap state and the Fermi level peak are strongly attenuated for a sample subject to an oxygen anneal (10^{-6} mbar for 30 min at 600 °C), as shown in the right hand panels of Figure 1, suggesting that they are interconnected. This result is in agreement with previous work using He(I) radiation ($h\nu = 21.2$ eV),[27] although the changes are much better defined in the current study.

In principle, two factors need to be considered to understand the changes in spectral intensity with photon energy. First, the electron inelastic mean free path increases with electron kinetic energy in the regime of our experiments from around 12 Å at 600 eV to 76 Å at 6000 eV,[34] so structure associated with states localized at or near the surface will be stronger at the lower photon energy, in the absence of other influences. Second, intensities are dependent on ionization cross-sections and the atomic make up of the electronic states involved. In particular, the cross-sections for ionizations of In 5s and In 5p states decrease with increasing photon energy much less rapidly than for O 2p states owing to the oscillatory behavior of the radial wavefunction close to the In nucleus.[35,36]

Qualitatively, it is possible to establish the influence of cross-section effects by reference to photoemission data for Sn-doped $In_2O_3(111)$ shown in Figure 2. The carrier density in
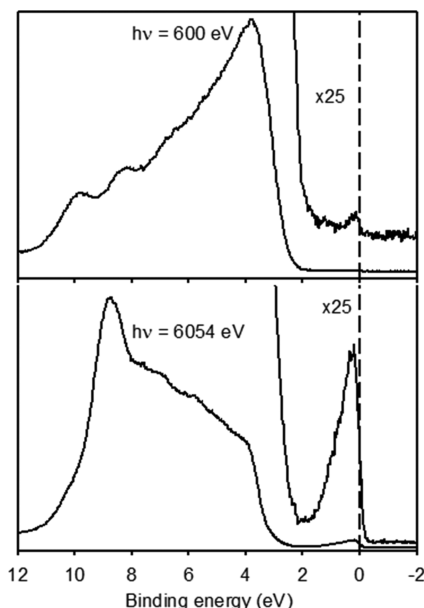
Figure 2. Hard and soft X-ray photoemission spectra of Sn-doped $In_2O_3(111)$. The increase in relative intensity of peaks at the bottom of the valence band and close to the Fermi energy provides a qualitative indication of the influence of cross-section effects.

this sample is estimated to be about 4.5×10^{20} cm^{-3} from the energy of the plasmon satellite observed on the In $3d_{5/2}$ core line (see Section 3.4 below).[29] At this high carrier density, the Fermi level lies above the charge neutrality level, and there is carrier depletion rather than carrier accumulation at the surface.[26] However, the Thomas−Fermi screening length is about 6.8 Å, so any band bending in the near-surface region must take place over this length range, which is less than the effective probing depth (which is usually considered to be 3 times the inelastic mean free path) for both the soft and hard X-rays used in the current study, as shown schematically in Figure 3. Thus, X-ray photoelectron spectroscopy (XPS) at both energies is dominated by the region where the electron gas is effectively homogenous (even at 600 eV, only 40% of the signal comes from the space charge region). The spectra in Figure 2 reveal an increase in intensity of the peak at the bottom of the valence band (as in Figure 1) and a related pronounced increase in the intensity of the conduction band peak near to the Fermi level. States at the bottom of the valence band and states in the conduction band both have pronounced In 5s character, and the intensity enhancement relative to states in upper part of the valence band reflects this high In 5s contribution.

Comparing Figures 1 and 2, it is apparent that the increase in the intensity of the conduction band feature is much less pronounced for the UHV-annealed sample of In_2O_3 than for Sn-doped In_2O_3. This is because in the former case, the conduction band peak derives from electrons in an accumulation whose overall thickness is of order 80 Å.[27] Thus, spectra excited at 600 eV photon energy are completely dominated by the space charge region, whereas at 6054 eV, the effective sampling depth in the experiment extends through the space charge layer into regions where the carrier density is
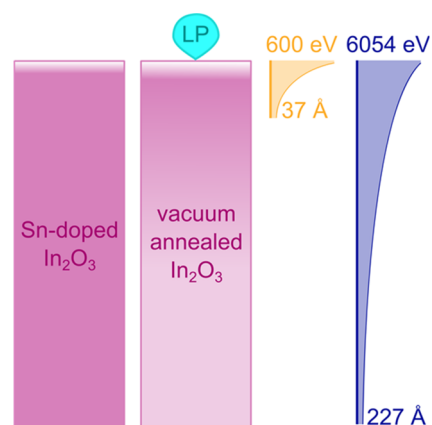
Figure 3. Schematic representation of the change of electron probing depth on increasing the photon energy from 600 to 6054 eV in relation to electron density in the electron-accumulation layer (indicated by the graded shading) formed on vacuum-annealed $In_2O_3(111)$ (1×1). Electron density in the surface lone pair is highlighted in cyan. The essentially homogenous electron density in Sn-doped In_2O_3 is also shown in a schematic. The exponential decrease in the contribution to the photoemission signal with increasing depth is indicated in the two curves on the right of the figure, which extend over a distance of 3 times the inelastic mean-free path.

much lower, as shown in the schematic diagram of Figure 3. Thus, the effects of cross-section changes are offset by the increase in sampling depth. At the same time, the intensity of the structure in the gap decreases dramatically relative to those of both the conduction band and the top of the valence band on increasing the photon energy from 600 to 6054 eV. Cross-section changes alone for a 5s−5p lone pair state would lead to an enhancement of the intensity relative to the top of the valence band, as is found in hard X-ray photoemission of the lone-pair state in SnO.[37,38] However, for states localized strongly on surface cations, cross-section effects will again be offset by changes in the effective sampling depth, to an extent that should be even more pronounced than when dealing with electrons in the accumulation layer. Thus, the existence of gap states entirely localized on the surface ad-atoms (suggested on the basis of STM measurements) explains the decrease in intensity of the gap state feature relative to the conduction band feature on increasing the photon energy. The present data are inconsistent with the previous suggestion that the gap states are associated with bulk oxygen vacancies.[27]

3.2. DFT Calculations. To provide atomistic insights into the nature of the surface states, we turned to first-principles calculations. Mapping of the potential energy surface for In ad-atoms on the surface of In_2O_3 reveals a number of 3-fold oxygen hollow sites as local energy minima, as shown Figure 4. More specifically, we may distinguish between A sites where the 3-fold oxygen hollow surrounds an oxygen atom at the bottom of the outer quadrupolar layer and B sites where this subsurface oxygen is missing, the subsurface sites would be occupied by an anion for (111) surfaces of materials with the stoichiometric MO_2 fluorite structure. The A and B sites have similar energies, although the adsorption minima are slightly deeper for the A sites (-0.45 eV) than the B sites (-0.32 eV). This small difference in energy is barely significant given the level of the DFT calculations.

The additional electron densities associated with ad-atoms in **A** and **B** adsorption sites are also shown in Figure 4. In both
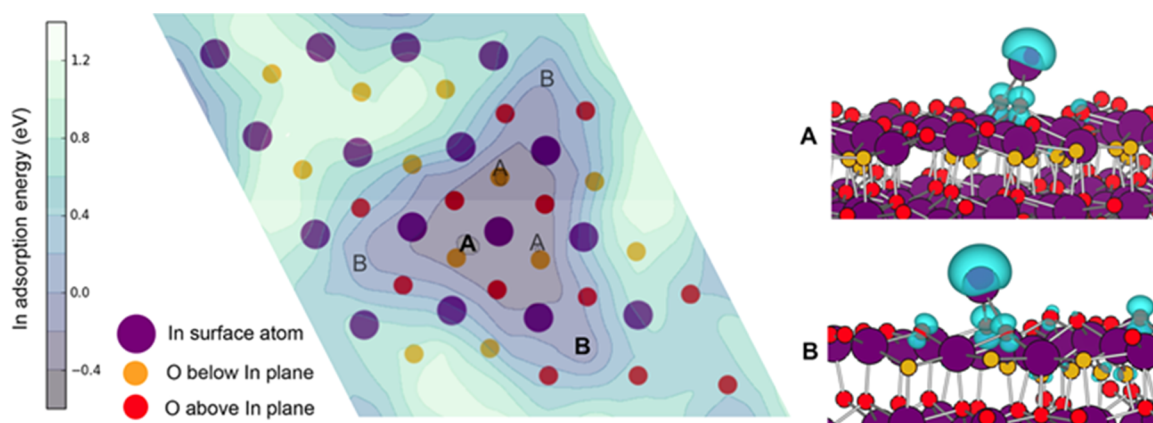
Figure 4. Calculated potential energy surface of single In ad-atom incorporation onto the (111) termination of In_2O_3. The adsorption energy is for the process: In(s) + bare-surface → In-on-surface. A number of local minima are found with a total energy within several meV of each other. Also plotted is the optimized relaxed surface structure after addition of an ad-atom for surface sites labeled A and B in the left hand panel, with the additional electron density superimposed in cyan.

cases, the electron density is mainly localized in an asymmetric lobe protruding out from the surface ad-atom, with a small contribution from adjacent oxygen atoms. This pattern of electron density is characteristic of a classical N-2 directional lone pair.

The partial densities of states (PDOS) for a bare slab and for a slab with a single uncompensated indium ad-atom per surface unit cell are shown in Figure 5. The In ad-atoms result in two changes to the electronic structure: (i) one electron is dispersed into the delocalized conduction band of In_2O_3 resulting in n-type doping and thereby the two-dimensional
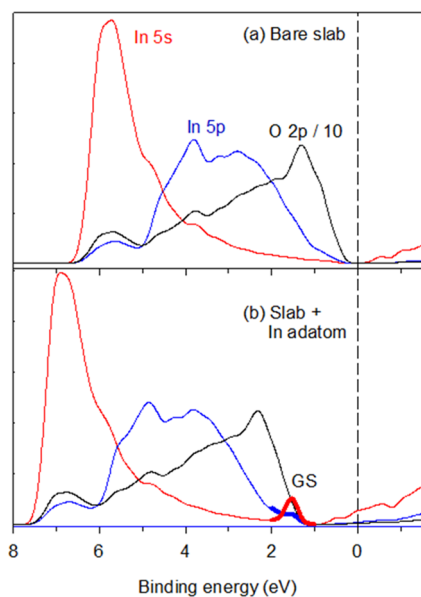
Figure 5. O 2p, In 5s, and In 5p partial densities of states (PDOS) for In_2O_3(111): (a) bare (1 × 1) slab, (b) after inclusion of a single In adatom in each surface unit cell in a B site. Binding energies are given relative to the Fermi level, which is indicated by the dashed line. The lower panel reveals the appearance of a new gap state (GS) just above the valence band maximum with mixed In 5s–5p character (identified in bold) and some O 2p characters as well as a shift in the Fermi level from midgap into the conduction band upon addition of the ad-atom. Note that the O 2p PDOS has been divided by 10 to allow visual comparison with In 5s and 5p states.

(2D) gas in the near surface region;[25−27] (ii) two electrons remain trapped in a state localized on the indium ad-atom. This state sits just above the main valence band edge and extends into the bulk bandgap. Inspection of the partial electronic densities of states shows that the gap state has pronounced In 5s and In 5p characters, as expected for a directional lone pair, but with additional mixing with O 2p states, as required by recent models for development of lone pairs.[9,10]

In the simple chemical nomenclature of the ionic model, the adatoms are N-2 valent In^+ ions, in contrast to In^{3+} formally present in the bulk. However, due to pronounced covalency, these different charge states are better represented as In(I) and In(III). Although the In(I) oxide In_2O is not known as a bulk solid phase, In_2O has been characterized in the gas phase.[39] A limited number of solid oxide phases containing In(I) are also known, including the tungsten bronze In_xWO_3[40] and In(I)-β''-alumina.[41] In_2O has also been deposited onto InAs(001) surfaces, where it was characterized by STM.[42] Thus, the formation of surface In(I) sites is broadly consistent with the known chemistry of indium. Lone-pair states of the sort we have identified are expected to have a profound impact on the catalytic[43] and photocatalytic activities of In_2O_3.[13] In particular, directional lone pairs will confer Lewis basicity on the surface indium sites, and at the same time the surface lone pairs, which lie just above the top of the bulk valence band, will act as centers for trapping photogenerated holes. Holes located at the surface are optimally placed to bring about oxidation reactions, such as the destruction of organic pollutants.[44]

3.3. LEED Analysis of the Surface Structure of Vacuum-Annealed In_2O_3(111). Figure 6 shows a LEED pattern from vacuum-annealed In_2O_3(111) surface taken during the course of the photoemission measurements on beamline I09. The pattern is characteristic of a (1 × 1) reconstruction, linking our present experiments to previous measurements of LEED I/V profiles for vacuum-annealed In_2O_3(111) (1 × 1). As mentioned previously, the earlier analysis of the LEED data assumed a simple bulk cut structure.[21] However, the new evidence from both STM[22] and the current photoemission measurements demands reanalysis of the existing LEED data set, with inclusion of ad-atoms as in the second (1 × 1) reconstruction proposed by Wagner et al.[22]
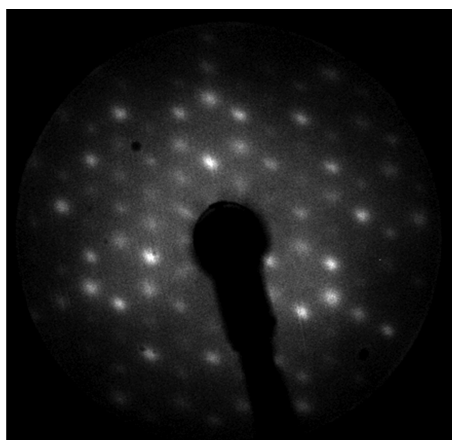
Figure 6. LEED pattern for vacuum-annealed $In_2O_3(111)$ measured on I09 at a beam energy of 69 eV. The pattern is characteristic of a (1×1) reconstruction.

Figure 7. Results of reanalysis of LEED I/V data from Pussi et al.[21] after inclusion of a single indium ad-atom in position B. The reanalysis leads to improvement of the Pendry R-factor from 0.31 without the ad-atom to 0.27.

Starting from a bulk cut structure, a single indium ad-atom was therefore added to one of the 3-fold hollow sites identified in the calculations discussed above, and relaxation was allowed in the outer two quadrupolar layers and for the In ad-atom. The geometrical parameters were optimized only in the vertical (z) direction: normal incidence LEED is not very sensitive to the lateral parameters, and the published data set was limited in range. In analyzing the LEED data, we were further constrained to deal with sites with local C_3 symmetry, i.e., all of the oxygen atoms were required to have the same z coordinate. Only one of the B sites met this requirement, and the subsequent discussion is based on occupation of this B site by the ad-atom. Although 81 atoms were therefore allowed to relax, symmetry constraints dictated that only 28 positional parameters were refined, along with the real part of the inner potential and the z coordinate of the ad-atom. This corresponds to $(1270/30)$ eV = 42 eV of raw data per parameter. All parameters were refined simultaneously.

Figure 7 shows the comparison between the measured LEED I/V profiles and the new best fit to the experimental data. The final Pendry R-factor was found to be 0.27 after inclusion of a single ad-atom per unit cell, as compared with R = 0.31 without ad-atoms. Although Figure 7 adheres to the conventional way of presenting LEED data in comparing measured and simulated I/V curves, it needs to be remembered that the Pendry R factor is defined in terms of the so-called "Y function", which depends on logarithmic derivatives of the intensity I. Optimizing the fit between measured and simulated plots of Y versus V gives emphasis to reproducing peak positions rather than peak intensities in the I/V curves. For indium atoms, the final error bars are between 0.03 and 0.06 Å in the outer quadrupolar layer and between 0.07 and 0.14 Å in the next layer. The error bars on the oxygen positions are larger and increase with depth below the surface from 0.07 to 0.10 Å in the outermost layer through ranges of 0.14–0.20; 0.20–0.30 and 0.30–0.30 Å in the next three layers. For some oxygen ions, no error bars could be defined because the R-factor curve was flat around the oxygen position. In summary then, the small improvement in R factor after inclusion of ad-atoms suggests that vacuum-annealed $In_2O_3(111)$ adopts the ad-atom (1×1) reconstruction rather than the simple bulk–cut structure assumed previously.
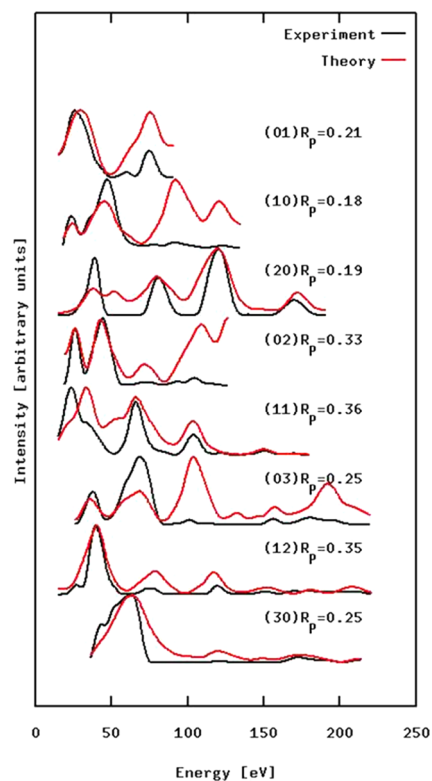
In the LEED analysis, three equal In–O bond lengths of 2.15 Å were found for the ad-atoms. In the DFT calculations, the allowance of lateral relaxation led to the ad-atom moving off-center in the hollow site to give three different and slightly longer In–O bond lengths of 2.28, 2.39, and 2.89 Å. The In–O bond length emerging from the LEED analysis is within the range between 2.13 and 2.23 Å found in the bulk crystal structure of In_2O_3.[45] Some of the discrepancies between LEED and DFT may arise from partial compensation the surface In(I) donors by near-surface oxygen interstitials, so that some of the ad-atoms are In(III) rather than In(I). Support for this idea is provided by consideration of the 2D electron density within the accumulation layer. Given a bulk lattice parameter of 10.117 Å, the presence of an In(I) one-electron donor within each surface unit cell would lead to a 2D electron density of 5.6×10^{13} cm^{-2} within the electron accumulation layer. The value inferred from measurements of the wavevector at the Fermi energy in angle-resolved photoelectron spectra is 4.2×10^{13} cm^{-2},[27] thus suggesting 25% of the donor centers is compensated. This would lead to reduction in the average In–O bond length. However, a more extended set of experimental LEED data, including measurements at non-normal incidence, is needed to further explore details of the surface structure, especially lateral relaxations.

3.4. Core-Level Photoemission Spectra. Core-level photoemission spectra in the In $3d_{5/2}$ and In $4d$ regions excited at 6054 eV photon energy are shown in Figure 8. The undoped oxygen-annealed sample gives a simple core line with a full width at half maximum height (FWHM) of 1.07 eV. Sn-doping gives distinct screened and unscreened final states typical for narrow band metallic oxides,[29,36,46−49] necessitating
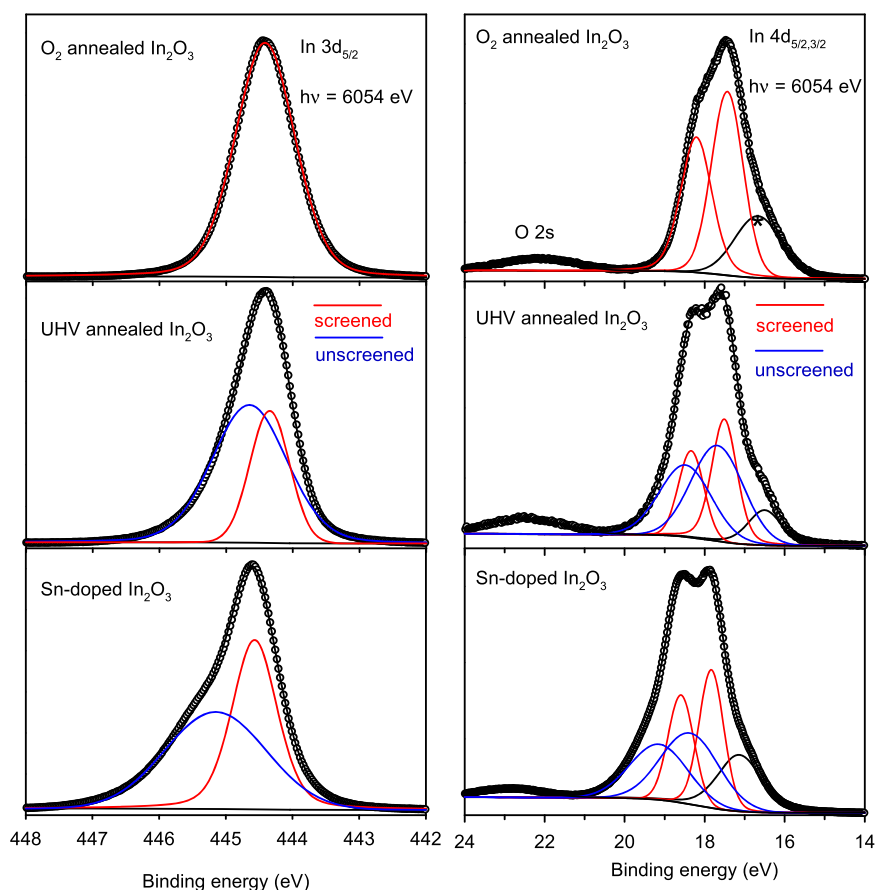
Figure 8. Comparison of $3d_{5/2}$ and In 4d structures in hard ($h\nu$ = 6054 eV) XPS for oxygen- and vacuum-annealed $In_2O_3(111)$ and Sn-doped $In_2O_3(111)$. The 4d spectrum involves overlapping $4d_{5/2}$ and $4d_{3/2}$ components, with a weak shoulder to the low binding energy side of the peak (identified with a * in the figure) associated with antibonding states arising from hybridization with deeper lying O 2s states.

a curve fit with two components. Recent first-principles calculations using many-body theory have shown that the high binding energy (unscreened) component may also be considered to be a plasmon satellite.[50] The plasmon energy of 0.60 eV for the core line is as expected for the nominal bulk doping level. Phonon broadening is suppressed in the screened peak, which is noticeably narrower (FWHM = 0.81 eV) than the single peak for the undoped sample. However, the unscreened final state peak (i.e., the plasmon satellite) is much broadened due to lifetime effects (FWHM = 1.78 eV). Plasmon satellite structure is also evident in the UHV-annealed sample, although the satellite energy of 0.31 eV is lower than for the bulk-doped sample: unlike in Sn-doped In_2O_3, the free carriers are confined to the accumulation layer, and the core line shape must represent an averaging of the screening response over the sampling depth of the experiment.

The In 4d for core line for oxygen-annealed In_2O_3 consists of overlapping $4d_{5/2}$ and $4d_{3/2}$ components, with a low binding energy shoulder arising from mixing with O 2s states found at slightly higher binding energy. For the oxygen-annealed sample, the individual spin-orbit components are somewhat narrower than for the Sn $3d_{5/2}$ core line (the FWHM values are 0.92 eV for both 5/2 and 3/2 components). Sn-doping again gives distinct screened and unscreened final states, with narrowing of the low binding energy component: the FWHM values are 0.74 eV for the screened peaks and 1.53 eV for the unscreened peaks, with a satellite energy of 0.54 eV similar to that for the In $3d_{5/2}$ core line. Again, satellites are

observed for the vacuum-annealed sample, with a lower energy separation (0.19 eV) from the low binding energy peaks than for the doped sample. Similar changes in the In $3d_{5/2}$ and In 4d spectra are found in the core lines under 600 eV excitation, but the peaks excited at the lower photon energy are all somewhat broader, and the spectra are less informative. This is probably due to the increased surface sensitivity. This means that the spectra are influenced more strongly by the effects of band bending and the strong variation in carrier density very close to the surface introduced by the surface potential barrier.[25−27] The spectra excited at 600 eV are therefore shown in Figure S2 in Supporting Information.

It might be expected that the presence of indium ad-atoms would give rise to a well-defined chemical shift in core level binding energies between the bulk In(III) and the surface In(I) adatoms. However, there is no evidence of a simple shift of this sort in addition to the plasmon satellite structure introduced by vacuum annealing discussed above. In fact, the issue of chemical shifts between N and N-2 states in post-transition metal compounds has proved controversial ever since Thomas and Tricker found in 1975 that there is essentially no chemical shift between Pb 4f core level binding energies for Pb(II) and Pb(IV) cations in the mixed valence oxide Pb_3O_4. In that system, it was argued that the expected shift due to the differing charges can be canceled by the 20 eV difference in site potential experienced by the Pb(II) cations (which occupy asymmetric three-coordinate sites) and the Pb(IV) cations (which occupy more regular six-coordinate sites).[51] Similarly,

Wertheim showed that the separation between O 1s and Sn 3d binding energies in Sn(II)O is essentially the same as in Sn(IV)O_2: once allowance is made for possible changes in the Fermi energy by comparing two core levels, there is no discernible chemical shift in the Sn 3d binding energy, again due to site potential effects.[52] Finally, there is a substantial body of high-quality XPS data for SnO_2 surfaces where a surface state appears in the bandgap of valence band spectra, (diagnostic of Sn(II) at the surface), but no obvious chemically shifted Sn(II) peak appears in Sn 3d or Sn 4d core XPS.[47,50,52,53]

The interplay between charge difference and site potentials in N/N-2 systems must be examined on a case-by-case basis. In the present context, DFT calculation allows us to explore the issue of chemical shift between In(I) and In(III) in an ab initio way by examining the shallow In 4d core level. Figure 9
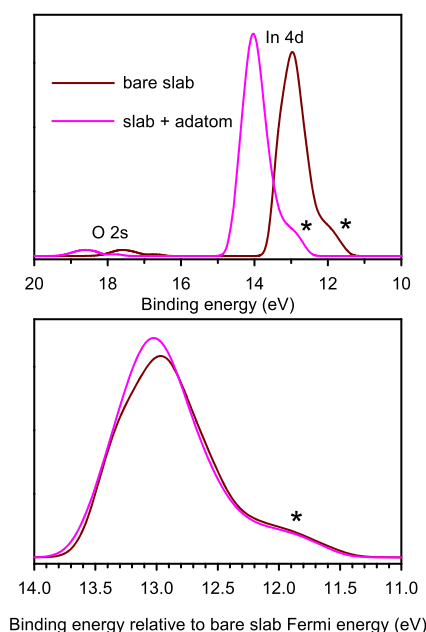
Figure 9. Upper panel: the In 4d partial density of states from DFT calculations on a bare $In_2O_3(111)$ slab and an $In_2O_3(111)$ slab with a single In adatom within each surface unit cell. The * symbol identifies antibonding states due to mixing of the shallow core 4d level with deeper lying O 2s states. In the bottom panel, the Fermi energy for the slab plus ad-atom has been shifted to coincide with the Fermi energy of the bare slab. The calculations do not include spin orbit splitting of the 4d levels, and DFT is unable to deal with the many-body screening response of electrons introduced into the conduction band by the ad-atoms.

shows the In 4d partial densities of states for a bare slab and for a slab after addition of In ad-atoms. As expected, introduction of In ad-atoms to both sides of the slab increases the total In 4d spectral weight. There is also a shift to high binding energy, as the Fermi energy moves from midgap up into the conduction band. However, there is little obvious change in the shape of the spectral profile, and when the core peaks are aligned to a common Fermi energy there is no evidence of a distinct chemical shift to low binding energy between In(I) ad-atoms and the In(III) atoms found in the bulk of the slab: if anything, the extra spectral weight associated with the ad-atoms appears slightly to the high binding energy side of the main peak. Thus, DFT tells us that there should be no discernible chemical shift in In 4d binding energies between

bulk In(III) and In(I) ad-atoms, in agreement with the experiments.

4. CONCLUDING REMARKS

The combination of hard and soft X-ray photoemission measurements performed in tandem with first-principles density functional theory calculations has established that electronic states found in photoemission spectra within the bandgap of $In_2O_3(111)$ arise from electron lone pairs localized on surface indium ad-atoms. These ad-atoms also provide the electrons for the well-known electron-accumulation layer that develops on the surface of In_2O_3 under reducing conditions.[26,27] The current interpretation differs from that advanced previously, where the gap state was presumed to arise from bulk oxygen vacancies and the electrons in the accumulation layer from surface oxygen vacancies.[27] This explanation is not consistent with hard and soft XPS when considered together. The current picture is much simpler and is supported by LEED I/V data, which confirm the presence of the ad-atoms first proposed on the basis of STM measurements. In earlier work, on a range of other In_2O_3 surfaces, including surfaces of polycrystalline films grown by sputtering techniques;[35,36] cubic $In_2O_3(001)$ grown by both MBE and metal organic chemical vapor deposition (MOCVD) on Y-doped $ZrO_2(001)$;[26] and rhombohedral $In_2O_3(0001)$ grown on $Al_2O_3(0001)$ by MOCVD,[26] gap state structure is always found hand-in-hand with electrons in an accumulation layer, as in the current work. This suggests that In ad-atoms may also be found on these surfaces. It remains to be seen if the ideas developed here can be extended to other post-transition metal oxides such as SnO_2[15,16] and Ga_2O_3[19] where in-gap states are also known to develop under reducing conditions. These gap states are usually assumed to involve trapping of two electrons associated with an oxygen vacancy on an adjacent cation but as has been shown in the current paper, ad-atoms provide an alternative source of electrons.

■ ASSOCIATED CONTENT

ⓢ Supporting Information

The Supporting Information is available free of charge on the ACS Publications website at DOI: 10.1021/acs.jpcc.8b08623.

STM images of UHV-annealed $In_2O_3(111)$ (1 × 1); In $3d_{5/2}$ and In 4d core level XPS excited at 600 eV photon energy (PDF)

■ AUTHOR INFORMATION

Corresponding Authors
*E-mail: A.regoutz@imperial.ac.uk (A.R.).
*E-mail: kelvin.zhang@xmu.edu.cn (K.H.L.Z.).
ORCID ⓘD
Daniel W. Davies: 0000-0003-4094-5992
Aron Walsh: 0000-0001-5460-7033
Anna Regoutz: 0000-0002-3747-3763
Kelvin H. L. Zhang: 0000-0001-9352-6236
Notes
The authors declare no competing financial interest.

■ REFERENCES

(1) Orgel, L. E. The stereochemistry of B-subgroup metals. 2. The inert pair. *J. Chem. Soc.* **1959**, 3815−3819.

(2) Dunitz, J. D.; Orgel, L. E. Stereochemistry of ionic solids. *Adv. Inorg. Chem. Radiochem.* **1960**, 2, 1.

(3) Walsh, A.; Watson, G. W. Electronic structures of rocksalt, litharge, and herzenbergite SnO by density functional theory. *Phys. Rev. B* **2004**, 70, No. 235114.

(4) Walsh, A.; Watson, G. W. Influence of the anion on lone pair formation in Sn(II) monochalcogenides: a DFT study. *J. Phys. Chem. B* **2005**, 109, 18868−18875.

(5) Walsh, A.; Watson, G. W. The origin of the stereochemically active Pb(II) lone pair: DFT calculations on PbO and PbS. *J. Solid State Chem.* **2005**, 178, 1422−1428.

(6) Walsh, A.; Watson, G. W.; Payne, D. J.; Edgell, R. G.; Guo, J. H.; Glans, P. A.; Learmonth, T.; Smith, K. E. Electronic structure of the alpha and delta phases of Bi_2O_3: a combined ab initio and X-ray spectroscopy study. *Phys. Rev. B* **2006**, 73, No. 235104.

(7) Raulot, J. M.; Baldinozzi, G.; Seshadri, R.; Cortona, P. An ab-initio study of the role of lone pairs in the structure and insulator-metal transition in SnO and PbO. *Solid State Sci.* **2002**, 4, 467−474.

(8) Waghmare, U. V.; Spaldin, N. A.; Kandpal, H. C.; Seshadri, R. First-principles indicators of metallicity and cation off-centricity in the IV-VI rocksalt chalcogenides of divalent Ge, Sn, and Pb. *Phys. Rev. B* **2003**, 67, No. 125111.

(9) Payne, D. J.; Egdell, R. G.; Walsh, A.; Watson, G. W.; Guo, J.; Glans, P. A.; Learmonth, T.; Smith, K. E. Electronic origins of structural distortions in post-transition metal oxides: experimental and theoretical evidence for a revision of the lone pair model. *Phys. Rev. Lett.* **2006**, 96, No. 157403.

(10) Walsh, A.; Payne, D. J.; Egdell, R. G.; Watson, G. W. Stereochemistry of post-transition metal oxides: revision of the classical lone pair model. *Chem. Soc. Rev.* **2011**, 40, 4455−4463.

(11) Lany, S.; Zakutayev, A.; Mason, T. O.; Wager, J. F.; Poeppelmeier, K. R.; Perkins, J. D.; Berry, J. J.; Ginley, D. S.; Zunger, A. Surface origin of high conductivities in undoped In_2O_3 thin films. *Phys. Rev. Lett.* **2012**, 108, No. 016802.

(12) Buckeridge, J.; Catlow, C. R. A.; Farrow, M. R.; Logsdail, A. J.; Scanlon, D. O.; Keal, T. W.; Sherwood, P.; Woodley, S. M.; Sokol, A. A.; Walsh, A. Deep vs. shallow nature of oxygen vacancies and consequent n-type carrier concentrations in transparent conducting oxides. *Phys. Rev. Mater.* **2018**, 2, No. 054604.

(13) Ghuman, K. K.; Hoch, L. B.; Szymanski, P.; Loh, J. Y. Y.; Kherani, N. P.; E-Sayed, M. A.; Ozin, G. A.; Singh, C. V. Photoexcited surface frustrated lewis pairs for heterogeneous photocatalytic CO_2 reduction. *J. Am. Chem. Soc.* **2016**, 138, 1206−1214.

(14) Batzill, M.; Diebold, U. The surface and materials science of tin oxide. *Prog. Surf. Sci.* **2005**, 79, 47−154.

(15) Cox, P. A.; Egdell, R. G.; Harding, C.; Patterson, W. R.; Tavener, P. J. Surface-properties of antimony doped tin(IV) oxide - a study by electron-spectroscopy. *Surf. Sci.* **1982**, 123, 179−203.

(16) Egdell, R. G.; Eriksen, S.; Flavell, W. R. Oxygen deficient $SnO_2(110)$ and $TiO_2(110)$ - a comparative-study by photoemission. *Solid State Commun.* **1986**, 60, 835−838.

(17) Themlin, J. M.; Sporken, R.; Darville, J.; Caudano, R.; Gilles, J. M.; Johnson, R. L. Resonant-photoemission study of SnO_2 - cationic origin of the defect band-gap states. *Phys. Rev. B* **1990**, 42, 11914−11925.

(18) Batzill, M.; Katsiev, K.; Burst, J. M.; Diebold, U.; Chaka, A. M.; Delley, B. Gas-phase-dependent properties of SnO_2 (110), (100), and (101) single-crystal surfaces: Structure, composition, and electronic properties. *Phys. Rev. B* **2005**, 72, No. 165414.

(19) Regoutz, A.; Egdell, R. G.; Morgan, D. J.; Palgrave, R. G.; Tellez, H.; Skinner, S. J.; Payne, D. J.; Watson, G. W.; Scanlon, D. O. Electronic and surface properties of Ga-doped In_2O_3 ceramics. *Appl. Surf. Sci.* **2015**, 349, 970−982.

(20) Panaccione, G.; Kobayashi, K. Hard X-ray photoemission spectroscopy: variable depth analysis of bulk, surface and interface electronic properties. *Surf. Sci.* **2012**, 606, 125−129.

(21) Pussi, K.; Matilainen, A.; Dhanak, V. R.; Walsh, A.; Egdell, R. G.; Zhang, K. H. L. Surface structure of $In_2O_3(111)$ (1×1) determined by density functional theory calculations and low energy electron diffraction. *Surf. Sci.* **2012**, 606, 1−6.

(22) Wagner, M.; Seiler, S.; Meyer, B.; Boatner, L. A.; Schmid, M.; Diebold, U. Reducing the In_2O_3 (111) surface results in ordered indium adatoms. *Adv. Mater. Interfaces* **2014**, 1, No. 1400289.

(23) Wagner, M.; Lackner, P.; Seiler, S.; Gerhold, S.; Osiecki, J.; Schulte, K.; Boatner, L. A.; Schmid, M.; Meyer, B.; Diebold, U. Well-ordered In adatoms at the $In_2O_3(111)$ surface created by Fe deposition. *Phys. Rev. Lett.* **2016**, 117, No. 206101.

(24) Zhang, K. H. L.; Payne, D. J.; Palgrave, R. G.; Lazarov, V. K.; Chen, W.; Wee, A. T. S.; McConville, C. F.; King, P. D. C.; Veal, T. D.; Panaccione, G.; et al. Surface structure and electronic properties of $In_2O_3(111)$ single-crystal thin films grown on Y-stabilized $ZrO_2(111)$. *Chem. Mater.* **2009**, 21, 4353−4355.

(25) King, P. D. C.; Veal, T. D.; Payne, D. J.; Bourlange, A.; Egdell, R. G.; McConville, C. F. Surface electron accumulation and the charge neutrality level in In_2O_3. *Phys. Rev. Lett.* **2008**, 101, No. 116808.

(26) King, P. D. C.; Veal, T. D.; Fuchs, F.; Wang, C. Y.; Payne, D. J.; Bourlange, A.; Zhang, H.; Bell, G. R.; Cimalla, V.; Ambacher, O.; et al. Band gap, electronic structure, and surface electron accumulation of cubic and rhombohedral In_2O_3. *Phys. Rev. B* **2009**, 79, No. 205211.

(27) Zhang, K. H. L.; Egdell, R. G.; Offi, F.; Iacobucci, S.; Petaccia, L.; Gorovikov, S.; King, P. D. C. Microscopic origin of electron accumulation in In_2O_3. *Phys. Rev. Lett.* **2013**, 110, No. 056803.

(28) Zhang, K. H. L.; Lazarov, V. K.; Veal, T. D.; Oropeza, F. E.; McConville, C. F.; Egdell, R. G.; Walsh, A. Thickness dependence of the strain, band gap and transport properties of epitaxial In_2O_3 thin films grown on Y-stabilised $ZrO_2(111)$. *J. Phys.: Condens. Matter* **2011**, 23, No. 334211.

(29) Bourlange, A.; Payne, D. J.; Palgrave, R. G.; Zhang, H.; Foord, J. S.; Egdell, R. G.; Jacobs, R. M. J.; Veal, T. D.; King, P. D. C.; McConville, C. F. The influence of Sn doping on the growth of In_2O_3 on Y-stabilized $ZrO_2(100)$ by oxygen plasma assisted molecular beam epitaxy. *J. Appl. Phys.* **2009**, 106, No. 013703.

(30) Walsh, A.; Catlow, C. R. A. Structure, stability and work functions of the low index surfaces of pure indium oxide and Sn-doped indium oxide (ITO) from density functional theory. *J. Mater. Chem.* **2010**, 20, 10438−10444.

(31) Van Hove, M. A.; Moritz, W.; Over, H.; Rous, P. J.; Wander, A.; Barbieri, A.; Materer, N.; Starke, U.; Somorjai, G. A. Automated-determination of complex surface-structures by LEED. *Surf. Sci. Rep.* **1993**, 19, 191−229.

(32) Materer, N.; Starke, U.; Barbieri, A.; Doll, R.; Heinz, K.; van Hove, M.; Somorjai, G. A. Reliability of detailed LEED structural-analyses − Pt(111) and Pt(111)-p(2 × 2). *Surf. Sci.* **1995**, 325, 207−222.

(33) Pendry, J. B. Reliability factors for LEED calculations. *J. Phys. C: Solid State Phys.* **1980**, 13, 937−944.

(34) Tanuma, S.; Powell, C. J.; Penn, D. R. Calculations of electron inelastic mean free paths. 5. Data for 14 organic compounds over the 50-2000 eV region. *Surf. Interface Anal.* **1994**, 21, 165−176.

(35) Walsh, A.; Da Silva, J. L. F.; Wei, S. H.; Korber, C.; Klein, A.; Piper, L. F. J.; DeMasi, A.; Smith, K. E.; Panaccione, G.; Torelli, P.; et al. Nature of the band gap of In_2O_3 revealed by first-principles

calculations and X-ray spectroscopy. *Phys. Rev. Lett.* **2008**, *100*, No. 167402.

(36) Körber, C.; Krishnakumar, V.; Klein, A.; Panaccione, G.; Torelli, P.; Walsh, A.; Da Silva, J. L. F.; Wei, S. H.; Egdell, R. G.; Payne, D. J. Electronic structure of In_2O_3 and Sn-doped In_2O_3 by hard X-ray photoemission spectroscopy. *Phys. Rev. B* **2010**, *81*, No. 165207.

(37) Ogo, Y.; Hiramatsu, H.; Nomura, K.; Yanagi, H.; Kamiya, T.; Kimura, M.; Hirano, M.; Hosono, H. Tin monoxide as an s-orbital-based p-type oxide semiconductor: electronic structures and TFT application. *Phys. Status Solidi A* **2009**, *206*, 2187−2191.

(38) Quackenbush, N. F.; Allen, J. P.; Scanlon, D. O.; Sallis, S.; Hewlett, J. A.; Nandur, A. S.; Chen, B.; Smith, K. E.; Weiland, C.; Fischer, D. A.; et al. Origin of the bipolar doping behavior of SnO from X-ray spectroscopy and density functional theory. *Chem. Mater.* **2013**, *25*, 3114−3123.

(39) Lakin, N. M.; van den Hoek, G.; Beattie, I. R.; Brown, J. M. The identification of In_2O in the gas phase by high resolution electronic spectroscopy. *J. Chem. Phys.* **1997**, *107*, 4439−4442.

(40) Ekström, T.; Parmentier, M.; Watts, K. A.; Tilley, R. J. D. Tungsten bronze formation by the group IIIA metals. *J. Solid State Chem.* **1984**, *54*, 365−377.

(41) Cetinkol, M.; Lee, P. L.; Wilkinson, A. P. Preparation and characterization of In(I)-beta-alumina. *Mater. Res. Bull.* **2007**, *42*, 713−719.

(42) Shen, J.; Melitz, W.; Feldwinn, D. L.; Lee, S.; Droopad, R.; Kummel, A. C. Bonding Geometries at the In_2O and SiO/III-V Semiconductor Interface. In *Physics and Technology of High-K Materials 8*; Kar, S., VanElshocht, S., Misra, D., Houssa, M., Landheer, D., Kita, K., Eds.; The Electrochemical Society, 2010; Vol. *33*, pp 105−116.

(43) Martin, O.; Martin, A. J.; Mondelli, C.; Mitchell, S.; Segawa, T. F.; Hauert, R.; Drouilly, C.; Curulla-Ferre, D.; Perez-Ramirez, J. Indium oxide as a superior catalyst for methanol synthesis by CO_2 hydrogenation. *Angew. Chem., Int. Ed.* **2016**, *55*, 6261−6265.

(44) Oropeza, F. E.; Davies, B.; Palgrave, R. G.; Egdell, R. G. Electronic basis of visible region activity in high area Sn-doped rutile TiO_2 photocatalysts. *Phys. Chem. Chem. Phys.* **2011**, *13*, 7882−7891.

(45) Marezio, M. Refinement of crystal structure of In_2O_3 at 2 wavelengths. *Acta Cryst.* **1966**, *20*, 723.

(46) Hill, M. D.; Egdell, R. G. The sodium tungsten bronzes - a study of the changes in electronic-structure with composition using high-resolution electron-spectroscopy. *J. Phys. C: Solid State Phys.* **1983**, *16*, 6205−6220.

(47) Egdell, R. G.; Rebane, J.; Walker, T. J.; Law, D. S. L. Competition between initial- and final-state effects in valence- and core-level X-ray photoemission of Sb-doped SnO_2. *Phys. Rev. B* **1999**, *59*, 1792−1799.

(48) Egdell, R. G.; Walker, T. J.; Beamson, G. J. The screening response of a dilute electron gas in core level photoemission from Sb-doped SnO_2. *J. Electron Spectrosc. Relat. Phenom.* **2003**, *128*, 59−66.

(49) Kahk, J. M.; Poll, C. G.; Oropeza, F. E.; Ablett, J. M.; Geolin, D.; Rueff, J. P.; Agrestini, S.; Utsumi, Y.; Tsuei, K. D.; Liao, Y. F.; et al. Understanding the electronic structure of IrO_2 using hard X-ray photoelectron spectroscopy and density-functional theory. *Phys. Rev. Lett.* **2014**, *112*, No. 117601.

(50) Borgatti, F.; Berger, J. A.; Ceolin, D.; Zhou, J. S.; Kas, J. J.; Guzzo, M.; McConville, C. F.; Offi, F.; Panaccione, G.; Regoutz, A.; et al. Revisiting the origin of satellites in core-level photoemission of transparent conducting oxides: the case of n-doped SnO_2. *Phys. Rev. B* **2018**, *97*, No. 155102.

(51) Thomas, J. M.; Tricker, M. J. Electronic-structure of oxides of lead. 2. Study of bulk rhombic PbO, tetragonal PbO, beta-PbO_2 and Pb_3O_4. *J. Chem. Soc., Faraday Trans. 2* **1975**, *71*, 329−336.

(52) Lau, C. L.; Wertheim, G. K. Oxidation of tin - ESCA study. *J. Vac. Sci. Technol.* **1978**, *15*, 622−624.

(53) Egdell, R. G.; Walker, T. J.; Beamson, G. The screening response of a dilute electron gas in core level photoemission from Sb-doped SnO_2. *J. Electron Spectrosc. Relat. Phenom.* **2003**, *128*, 59−66.